

## Feasibility of induced polarization effects in time-domain airborne EM data

**Seogi Kang**

University of British Columbia,  
Geophysical Inversion Facility  
Vancouver, BC, Canada  
skang@eos.ubc.ca

**Douglas W. Oldenburg**

University of British Columbia,  
Geophysical Inversion Facility  
Vancouver, BC, Canada  
doug@eos.ubc.ca

**Lindsey J. Heagy**

University of British Columbia,  
Geophysical Inversion Facility  
Vancouver, BC, Canada  
lheagy@eos.ubc.ca

### SUMMARY

The potential for extracting and interpreting induced polarization (IP) data from airborne surveys is now broadly recognized. There is, however, still considerable discussion about the conditions under which the technique can provide knowledge about the subsurface and thus its practical applications. Foremost among these is whether, or under what conditions, airborne IP can detect chargeable bodies at depth. We focus on data obtained from a coincident loop time-domain system. Our analysis is expedited by using a stretched exponential rather than a Cole-Cole model to represent the IP phenomenon. Our paper begins with an example that illuminates the physical understanding about how negative transients (the typical signature of the airborne IP) can be generated. The effects of the background conductivity are investigated and this shows that a moderately conductive and chargeable target in a resistive host is an ideal scenario for generating strong IP signals. We then address the important topic of estimating the maximum depth of the chargeable target that can generate negative transients.

**Key words:** Induced Polarization, Airborne EM, Time-domain

### INTRODUCTION

Earth rocks are chargeable because they can act as capacitors when an electric field is applied by an electromagnetic (EM) source such as grounded electrodes. This is often called the induced polarization (IP) phenomenon. Rocks can have different polarization mechanisms which results in different IP characteristics as a function of frequency. This can be translated into a complex conductivity model such as the Cole-Cole conductivity model (Tarasov, 2013):

$$\sigma_{cc}(\omega) = \sigma_{\infty} - \sigma_{\infty}\eta_{cc} (1 + (i\omega\tau_{cc})^{c_{cc}})^{-1} \quad (1)$$

where  $\sigma_{\infty}$  is the conductivity at infinite frequency,  $\eta_{cc}$  is the chargeability,  $\tau_{cc}$  is the time constant (s), and  $c_{cc}$  is the frequency exponent; subscript CC indicates Cole-Cole.

IP surveys have been successfully conducted in a variety of geoscience applications. For mining, IP surveys are recognized as a principal geophysical technique for finding disseminated sulphides or porphyry deposits. Non-metallic materials such as clays and ice can also generate IP signals, making IP a useful technique in a range of environmental applications. Grounded DC-IP surveys have been successfully used for both mining and environmental applications for the past decades. Airborne EM (AEM) systems can also measure IP signals. In particular time-domain AEM surveys using a coincident-loop system sometimes display a negative transient; this is a distinctive IP signature. Compared to the EM signals, these negatives (IP signals) have much smaller amplitudes and hence, for the initial AEM systems, it was not clear if the measured negatives were signals from chargeable materials or they were simply noise

generated by power lines or electric fences (Smith and Klein, 1996). With time however, instruments have improved and the validity of negative transients as signal was firmly established (Macnae, 2015; Viezzoli and Kaminski, 2017). For instance, consistent negatives were recorded over the Tli Kwi Cho kimberlite deposit with three different AEM systems (Kang et al., 2017). As the quality of the instrumentation improves, it is expected that the more IP signals can be measured in airborne data. This ability to measure airborne IP signals has raised considerable motivation for developing a methodology that can extract chargeability information from airborne IP data. Various approaches, including simple curve-fitting, 1D inversions, and 3D inversions have been developed and successfully applied to field examples. Therefore, there is a significant enthusiasm for the potential use of the airborne IP techniques in a variety of applications (e.g. mining and groundwater). However, setting proper expectations about the technique and recognizing its limitation based upon the physics and the current system specifications is crucial, because neither overselling nor underselling the technique is beneficial for the community.

Macnae (2015) investigated the physics of airborne IP and its practical aspects using a simple thin-sheet solution and a main conclusion from his study was that airborne IP is only a surficial clay mapper (< 100 m). Viezzoli and Kaminski (2017), however, showed the potential that a deeper chargeable target, such as a mineral deposit (> 100 m), can be detected, but that work was based upon analysis using 1D simulations. Hence, there is disagreement about the potential depth of investigation of the airborne IP technique. Although the approximate thin-sheet solution and semi-analytic 1D solutions used respectively in Macnae (2015) and Viezzoli et al. (2017) can illustrate some meaningful concepts with respect to airborne IP, these approaches are limited in their ability to model the physics in the presence of complex conductivity structures. For instance, any galvanic (or channelled) currents are not taken into account in either approach. Investigating the feasibility of airborne IP in realistic geologic settings requires the use of 3D numerical simulations that solve the full Maxwell's equations with a more complicated conductivity model.

In this paper, we first develop a convolutional time-domain EM (TEM) simulation code using a stretched exponential (SE) conductivity function (Kohlrausch, 1854). We then use this code to investigate three main questions related to the feasibility of the airborne IP technique:

- How does chargeable material in the subsurface generate negative transients in coincident loop systems?
- How does the background conductivity affect the IP signals?
- To what depth can we expect to detect a chargeable body?

## SIMULATING AIRBORNE IP DATA USING A STRETCHED EXPONENTIAL

With a complex conductivity,  $\sigma(\omega)$ , the current density,  $\vec{j}$ , in the frequency domain, can be written as:

$$\vec{j} = \sigma(\omega)\vec{E} \quad (2)$$

where  $\vec{E}$  is the electric field (V/m). In the time-domain, the current density,  $\vec{j}$ , is:

$$\vec{j} = \sigma(t) \otimes \vec{e} \quad (3)$$

where  $\otimes$  is a causal convolution ( $t > 0$ ). Then Maxwell's equations can be written as

$$\nabla \times \vec{e} = -\partial \vec{b} / \partial t \quad (4)$$

$$\nabla \times \mu^{-1} \vec{b} - \vec{j} = \vec{j}_s \quad (5)$$

where  $\vec{b}$  is the magnetic flux density (Wb/m<sup>2</sup>) and  $\vec{j}_s$  (A/m<sup>2</sup>) is the current source, and  $\mu$  is the magnetic permeability (H/m). By discretizing and solving the above equations in 3D, we can compute TEM data that include IP effects (Marchant, 2015). For the discretization of eqs. (3)-(5), an open-source geophysical simulation and inversion package, SimPEG, is used (Cockett et al., 2015). The developed SimPEG-EMIP code works for both 3D tensor meshes and 2D/3D cylindrical meshes (Heagy et al., 2017).

For a time-dependent conductivity,  $\sigma(t)$ , we use the stretched exponential (SE) model rather than the Cole-Cole model defined in the frequency-domain (eq. 1). The SE conductivity for a step-off function,  $1-u(t)$ , can be written as

$$\sigma_{se}(t) \otimes [1-u(t)] = -\sigma_{\infty} \eta_{se} \exp[-(t/\tau_{se})^{c_{se}}] \quad (6)$$

where  $u(t)$  is the Heaviside step function, and subscript SE stands for stretched exponential. Taking the derivative with respect to time and multiplying by -1 yields

$$\sigma_{se}(t) = \sigma_{\infty} \delta(t) - \sigma_{\infty} \eta_{se} c_{se} t^{-1} (t/\tau_{se})^{c_{se}-1} \exp[-(t/\tau_{se})^{c_{se}}] \quad (7)$$

A main reason why we used the SE conductivity function rather than the Cole-Cole function is its numerical advantage for the convolutional algorithm. With the SE conductivity, which has an explicit form in time-domain, we do not need to convert  $\sigma(\omega)$  within each discretized voxel to  $\sigma(t)$ . The SE conductivity will not be beneficial when Maxwell's equations are solved in frequency-domain in the same manner, and we believe that is the reason why the SE conductivity has not been used extensively except for the latest simulation study from Belliveau and Haber (2017).

Although the SE conductivity is not exactly the same as Cole-Cole conductivity (eq. 1), their time features are very similar, and when  $c_{cc}=1$  (Debye model), they are equivalent. To illustrate cases when  $c_{cc}$  is not equal to 1, we fit the Cole-Cole conductivity with the SE conductivity in time-domain. Fig. 1 shows example Cole-Cole conductivity decays ( $t > 0$ ) with variable  $c_{cc}$ , and their fits with the SE conductivity. For the range of time of interest in the current AEM system ( $10^{-3}$ - $10^1$  ms), the SE function effectively fits the Cole-Cole, as shown in Fig. 1;  $\tau_{se}$  is coincident with  $\tau_{cc}$  whereas  $\eta_{se}$  and  $c_{se}$  slightly underestimate  $\eta_{cc}$  and  $c_{cc}$  respectively. Therefore, when interpreting the SE parameters, the readers can use their understanding based upon Cole-Cole parameters and treat the SE and CC parameters as being equivalent.

## NUMERICAL EXPERIMENTS

To answer the three questions posed previously, we carry out TEM simulations using the SimPEG-EMIP code. For the spatial discretization, we use the 2D cylindrically symmetric mesh because of the cylindrical symmetry in the time-domain AEM

system, which uses a horizontal loop (See Fig. 2). A step-off waveform is used for the input current and a horizontal receiver loop measuring the voltage (equivalent to  $-db_z/dt$ ) is coincident with the source loop. Data are measured in the off-time over the time-range:  $10^{-2}$ -10 ms. A chargeable cylinder is embedded in the resistive half-space ( $\sigma_{half}=10^{-3}$  S/m). The depth to the top ( $z$ ), radius ( $r$ ), thickness ( $h$ ) of the chargeable cylinder are correspondingly  $z=50$  m,  $r=200$  m,  $h=100$  m; the SE parameters of the cylinder are  $\sigma_{\infty}=0.1$  S/m,  $\eta_{se}=0.1$ ,  $\tau_{se}=10^{-3}$  s,  $c_{se}=0.7$ ; the cylinder is 100 times more conductive than the half-space and its effective conductance ( $\sigma h$ ) is 10 S.

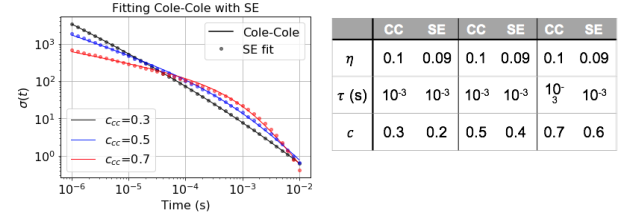


**Figure 1. Left: the stretched exponential (SE) fit of the Cole-Cole conductivity in the time domain. Solid lines are the impulse response using a Cole-Cole representation and the circles denote the SE response. Black, blue, and red colors correspondingly indicates when  $c_{cc}$  are 0.3, 0.5, and 0.7. Right: comparison of the Cole-Cole and the resultant SE parameters for variable  $c_{cc}$ .**

To understand how negative transients are caused by the presence of chargeable rocks, we first explore how the electric field diffuses into the earth after the input current is turned off. Fig. 3 shows the simulated electric field in y-direction (into the page) at four different time channels (0.01-7.94 ms). At early times (0.01-0.3 ms), electric fields which rotate in the horizontal plane in a counter-clockwise direction are induced in both the half-space and in the conductive cylinder. As time passes, the electric field diffuses downwards and radially outwards; particularly large rotating electric fields are induced in the conductor. These inductive currents are responsible for “charging up” the earth material. At a later time (7.94 ms), the inductive currents have gone and only the decaying polarization currents remain. The resultant electric fields (and currents) have a reversed direction and these will generate negative voltages at the receiver location. The black lines in Fig. 4(a) show the measured time decays,  $d^{obs}$ , (on a log-log scale); negative values are shown after 2 ms (black dashed line). Another simulation is carried out without IP effects ( $\eta_{se} = 0$ ), and the computed data are shown with the blue line (no negatives); we call these the fundamental data,  $d^F$ , which include only EM induction effects. The IP data,  $d^{IP}$ , can simply be defined as

$$d^{IP} = d^{obs} - d^F \quad (8)$$

The system noise-level is set to  $10^{-4}$  pV/Am<sup>2</sup> based upon Viezzoli and Kaminski (2017), and the values below the noise-level are not shown. At the early times ( $< 1$  ms),  $d^{obs}$  and  $d^F$  are almost coincident indicating that EM induction dominates the response. On the other hand, IP effects are dominant at later times ( $> 2$  ms). To show the relative strength of the IP effects, we define the ratio, R, between  $|d^F|$  and  $|d^{IP}|$ :

$$R = |d^{IP}| / |d^F| \quad (9)$$

We show R in Fig. 4(b); ratios smaller than 0.1 are ignored. After 1 ms R is greater than 0.1, indicating that there are considerable IP effects in the observations. When R=1, the observation is zero which corresponds to the time that the sign reversal occurs.

The EM induction processes within the background conductivity structure influence the electric field, which serves

as a forcing function for IP effects, at the target. These IP effects are translated into the reversed direction of the electric field which results in negative transients that are observed after the EM induction effects have decayed. In the following sections, we carry out TEM-IP simulations varying the model parameters shown in Fig. 2 to systematically investigate the feasibility of the airborne IP technique.

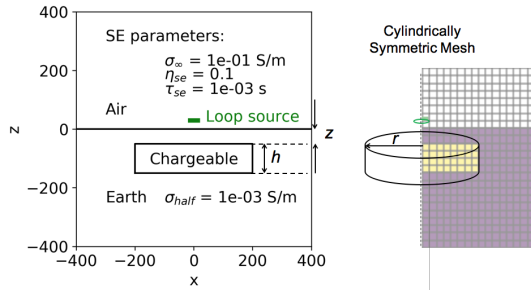


**Figure 2.** A chargeable cylinder embedded in a half-space earth. The 13m-radius source loop is located 30 m above the surface. The depth to the top of the prism is denoted by  $z$ . Right: the 2D cylindrically symmetric mesh is used for TEM simulations.

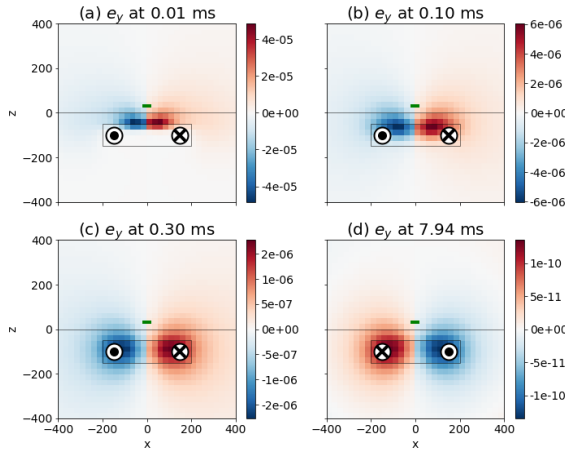


**Figure 3.** Electrical fields diffusing in the earth; the chargeable cylinder is outlined in black. At early times (0.01-0.3 ms), EM induction is dominant resulting in inductive electric fields rotating counter-clockwise direction. However, at 7.94 ms the reversed direction (clockwise) of the electric field is generated due to the chargeable cylinder.

### Effects of background conductivity on IP signals

As we demonstrated in Fig 3, the electric fields are the forcing function which generate IP signals. Understanding the effects of the background conductivity on these electric fields is therefore crucial for understanding the resultant IP signals. To investigate this, we perform TEM-IP simulations for a range of values of  $\sigma_{half}$  and  $\sigma_{\infty}$ . Other parameters for the simulation setup are the same as those in Fig. 1 ( $r=200$  m,  $h=100$  m,  $z=50$  m,  $\eta_{se} = 0.1$ ,  $\tau_{se}=10^{-3}$  s).

The first experiment involves varying  $\sigma_{\infty}$ , which ranges from  $10^{-4}$  S/m to 1 S/m, while  $\sigma_{half}$  is fixed to  $10^{-3}$  S/m. Figs. 5(a) and (b) show time decays of the observation and corresponding ratios,  $R$ . Negative transients are only visible when  $\sigma_{\infty}$  is 0.01 S/m and 0.1 S/m (red and green curves). When  $\sigma_{\infty}$  is too high (e.g. 1 S/m), EM effects dominate at all times and no negative transients are visible in the observed data. At the other end of the spectrum, the very resistive target shows the smallest  $R$ . These results show us that a moderately conductive target provides the best opportunity for observing negative transients

in the data. When  $\sigma_{half} = \sigma_{\infty}$ , there are no negatives in the time decay curve, but the observation includes some IP effects after 1 ms with small strength ( $R < 0.2$ ).

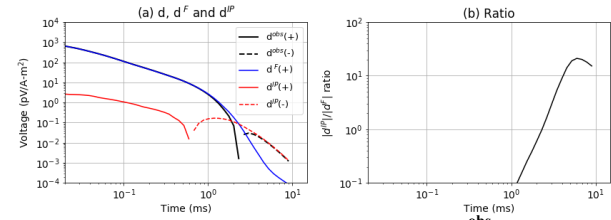


**Figure 4.** (a) Simulated TEM responses;  $d^{obs}$  (black) are observations (EM+IP),  $d^F$  (blue) are fundamental (EM) data, and  $d^{IP}$  (red) are IP data. Solid and dashed lines distinguish positive and negative values. (b)  $R = |d^{IP}| / |d^F|$  shows the relative strength of the IP signals compared to the fundamental induction effects.

To explore the effect of the half-space conductivity, we fix the ratio,  $\sigma_{\infty} / \sigma_{half}$  to 10, and change  $\sigma_{half}$  from 0.1 S/m to  $10^{-4}$  S/m. In Fig. 6, negatives are present when  $\sigma_{half}$  is  $10^{-4}$  S/m and  $10^{-3}$  S/m, but not for the other cases. This shows that when the half-space conductivity is too high (0.1 S/m) measuring IP signals will be challenging even though chargeable material exist. Therefore, a moderately conductive target ( $\sim 0.01$ -0.1 S/m) in a resistive host ( $\sim 10^{-4}$ - $10^{-3}$  S/m) provides the best circumstances for observing strong IP signals.

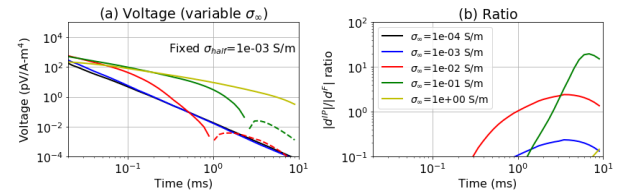


**Figure 5.** (a) Time decay curves with a variable conductivity of the chargeable cylinder ( $\sigma_{\infty}$ ). Solid and dashed lines distinguish positive and negative values. The half-space conductivity is fixed at  $10^{-3}$  S/m, whereas varies ( $10^{-4}$ -0.1 S/m) as shown in the legend in (b) which plots the  $|d^{IP}| / |d^F|$  ratio,  $R$ .

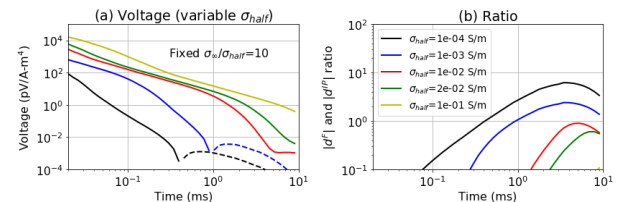


**Figure 6.** (a) Time decay curves with a variable conductivity of the half-space ( $\sigma_{half}$ ). Solid and dashed lines distinguish positive and negative values. The ratio between  $\sigma_{half}$  and the target conductivity,  $\sigma_{\infty}$ , is fixed to 10, whereas  $\sigma_{half}$  varies ( $10^{-4}$ -0.1 S/m) as shown in the legend in (b) which displays the  $|d^{IP}| / |d^F|$  ratio,  $R$ .

### To what depth can we expect to detect chargeable rocks with airborne IP?

Often, the maximum depth that airborne IP can see chargeable targets is considered to be fairly low ( $\sim 100$  m from Macnae, 2015). However, the possibility exists to see deeper when the host is resistive and the chargeable target is moderately conductive. Here we explore detectability of a chargeable target by altering the depth of the chargeable cylinder ( $z$ ) from 0-350 m. Fig. 7 shows the time decays with variable  $z$  when  $\sigma_{\infty}$  and  $\sigma_{half}$  are 0.1 S/m and  $10^{-3}$  S/m. Negatives are present when  $z \leq 200$  m. By decreasing  $\sigma_{half}$ , this depth can be increased to 300 m as shown in Fig. 8. Hence, it is possible to detect a deeper chargeable target using the airborne IP technique when the target is moderately conductive and the host rocks is resistive



( $10^{-4}$  S/m). For instance, at Tli Kwi Cho kimberlite deposit negatives were measured near a kimberlite pipe. This moderately conductive pipe was embedded in a resistive host rock ( $10^{-4}$  S/m); it was located  $\sim 70$  m below the surface and its radius and thickness were about 150 m and 200 m, respectively (Kang et al, 2017).

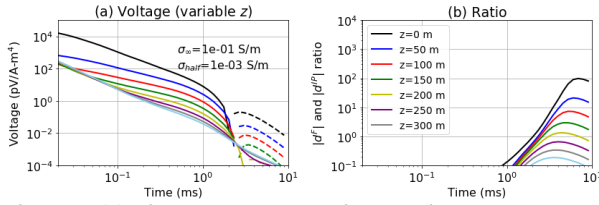


**Figure 7. (a) Time decay curves with a variable target depth ( $z$ ) ranging from 0-350 m. The half-space conductivity is  $10^{-3}$  S/m. (b)  $|d^IP|/|d^F|$  ratio, R.**

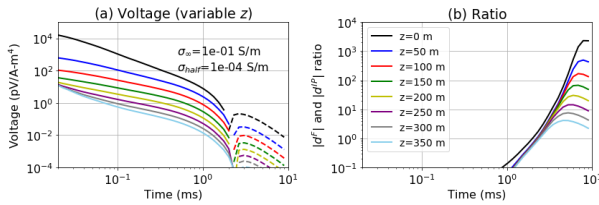


**Figure 8. (a) Time decay curves with a variable target depth ( $z$ ) ranging from 0-350 m. The half-space conductivity is decreased to  $10^{-4}$  S/m compared to Fig. 7. (b)  $|d^IP|/|d^F|$  ratio, R.**

#### The effects of target size

The examples shown so far have illustrated general principles concerned with the ability to detect IP bodies at depth. We have dealt with a specific geometry and have worked with a fairly large target. The strength of the IP signal depends upon the size and geometry of the target. To begin an exploration of the impact of target size on detectability, we show the effects of making the body smaller. We first reduce the radius ( $r$ ) from 200 m to 50 m. As a result, the maximum depth has decreased to 200 m as shown in Fig. 9. We can also reduce the thickness ( $h$ ), as shown in Fig. 10; here  $z=150$  m and  $r=100$  m. When  $h \leq 30$  m, we no longer observe the negatives. Depending on the geological setting, more complicated situations may occur and the potential for seeing an IP signal in the airborne data will require 3D modelling appropriate to the geology.

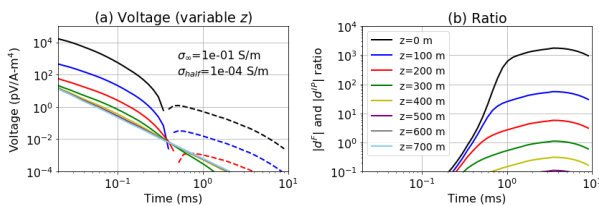


**Figure 9. (a) Time decay curves with a variable target depth ( $z$ ). The radius of the chargeable cylinder is decreased from 200 m to 100 m compared to Fig. 8. (b)  $|d^IP|/|d^F|$  ratio, R.**

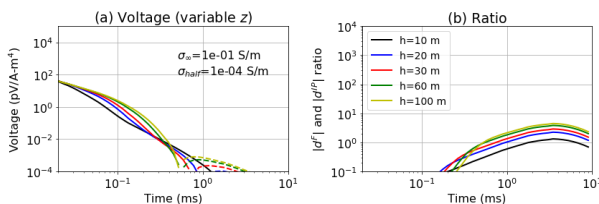


**Figure 10. (a) Time decay curves with a variable target thickness ( $h$ ). The radius ( $r$ ) and depth to the top ( $z$ ) of the chargeable cylinder are fixed to 50 m and 150 m, respectively, whereas  $h$  varies (1-100 m) as shown in the legend in (b) which displays the  $|d^IP|/|d^F|$  ratio.**

## CONCLUSIONS

We have developed a convolutional TEM simulation code that directly solves Maxwell's equations in time with the SE (stretched exponential) conductivity function. The SE conductivity is a good representation of the Cole-Cole conductivity for the typical time range used in AEM. With our simulations we showed that:

- Negative transients in AEM data are caused by the reversed direction of the electric field in a chargeable target and are visible at late times when EM induction is small.
- Moderately conductive targets ( $0.01$ - $0.1$  S/m) in a resistive host ( $10^{-4}$ - $10^{-3}$  S/m) show the best potential for generating strong IP signals (negatives).
- The depth at which we can detect a target with airborne IP depends upon the background conductivity, but for an ideal situation (a conductive, chargeable target in a resistive host), the target can be detected up to 300 m depth.
- The strength of the IP signals and the depth of detectability of a target is dependent upon the size of the target and its geometry. In general 3D simulations, cast within the relevant geologic context, are required.

The question of overriding practical concern is whether, or under what circumstances, you can see an IP target at depth in airborne EM data. The situation is complex and cannot be answered by a simple, fixed depth of investigation rule. Forward simulation which emulates the potential geology, is required. To advance this capability, we have developed the SimPEG-EMIP codes as a part of the open-source software project, SimPEG (<http://simpeg.xyz>). The main workhorse for this paper has been the 2D cylindrical mesh, and the figures in this text can be reproduced ([https://github.com/simpeg-research/kang\\_2018\\_AEMworkshop](https://github.com/simpeg-research/kang_2018_AEMworkshop)). Moreover, the source code is downloadable and users can explore the use of different parameters. We hope contributes to the wider challenge of extracting IP information from airborne time-domain EM data.

## REFERENCES

- Belliveau, P. and Haber E., 2018. Coupled simulation of electromagnetic induction and induced polarization effects using stretched exponential relaxation: *Geophysics*, 83, WB109-WB121.
- Cockett, R., Kang, S., Heagy, L., Pidlisecky, A., and Oldenburg, D., 2015, SimPEG: An open source framework for simulation and gradient based parameter estimation in geophysical applications: *Computers & Geosciences*, 85, 142-154.
- Heagy L., Cockett, R., Kang, S., Rosenkjaer, G., and Oldenburg, D., 2017, A framework for simulation and inversion in electromagnetics: *Computers & Geosciences*, 107, 1-19.
- Kang S. and Oldenburg, D. W., 2016, On recovering distributed IP information from inductive source time domain electromagnetic data, *Geophysical Journal International*, 207, 174-196.
- Kohlrausch, 1854, Theorie des elektrischen Rückstandes in der Leidener Flasche: *Annalen der Physik*, 167, 179-214.
- Macnae, J., 2015, Quantifying Airborne Induced Polarization effects in helicopter time domain electromagnetics: *Journal of Applied Geophysics*, 135, 495-502.
- Marchant, D., 2015: Induced polarization effects in inductive source electromagnetic Data, Ph.D. Thesis, University of British Columbia.
- Smith, R. and Klein, J., 1996, A special circumstance of airborne induced- polarization measurements: *Geophysics*, 61, 66-73.
- Tarasov, A. and Titov, K., 2013, On the use of the Cole-Cole equations in spectral induced polarization: *Geophysical Journal International*, 195, 352-3